CHAPTER 13: MATERIALS CONSIDERATIONS AND DATA BASE

Contributors

Lead Author: S.J. Zinkle
S. Majumdar
N.M. Ghoniem
S. Sharafat.

13. MATERIALS CONSIDERATIONS AND DATA BASE

13.1 Introduction

A wide range of structural materials was originally considered for the APEX project. This list included conventional materials (e.g., austenitic stainless steel), low-activation structural materials (ferritic-martensitic steel, V-4Cr-4Ti, and SiC/SiC composites), oxide dispersion strengthened ferritic steel, conventional high temperature refractory alloys (Nb, Ta, Mo, W alloys), Ni-based super alloys, ordered intermetallics (TiAl, Fe_3Al, etc.), various composite materials (C/C, Cu-graphite and other metal-matrix composites, Ti_3SiC_2, etc.), and porous-matrix metals and ceramics (foams). In order to provide maximum flexibility in the design (and to increase the possibility for significant improvements in reactor power density), low long-term activation was not used as a defining "litmus test" for the selection of candidate materials.

Due to limitations in resources and time, the materials analysis for APEX quickly focused on refractory alloys due to their higher thermal stress capacity and higher operating temperature capabilities compared to conventional structural materials (see below). However, it should be emphasized that conventional materials may work satisfactorily in some of the APEX concepts (e.g., austenitic stainless steel located behind a thick wall of Flibe). Other promising advanced structural materials (e.g., oxide dispersion strengthened alloys, intermetallics) should be considered in future analyses.

Numerous factors must be considered in the selection of structural materials, including

- unirradiated mechanical and thermophysical properties
- chemical compatibility and corrosion
- material availability, cost, fabricability, joining technology
- radiation effects (degradation of properties)
- Safety and waste disposal aspects (decay heat, etc.)

Information assembled by the APEX team during past 18 months on the first four items in this list is summarized in this chapter.

13.1.1 Material costs and fabrication issues

The APEX materials team gathered information on the costs of many of the candidate structural materials. This raw material cost information is summarized in Table 13.1. The fabrication costs for producing finished products of refractory alloys (particularly W) is known to be much higher than for steels. The Group V refractory metals (V, Nb, Ta) are relatively easy to fabricate into various shapes such as tubing, whereas the Group VI refractory metals (Mo, W) are very difficult to fabricate. A further issue with all of the refractory metals is joining, particularly in-field repairs. Satisfactory

full-penetration welds have not been developed for W, despite intensive efforts over a >25 year time span (1960-1985). The main issue associated with fusion zone welding of the Group V alloys is the pickup of embrittling interstitial impurities (O, C, N, H) from the atmosphere. Work is in progress to develop satisfactory fusion welds for vanadium alloys. One promising alternative joining technique that has recently been developed by the aerospace industry is stir friction welding. Since this is a solid-state joining technique, the pickup of atmospheric impurities should be reduced compared to conventional weld techniques. An additional potential benefit (yet to be demonstrated) is the possibility of repair-welding irradiated materials containing >10 appm He.

Table 13.1 Costs for simple plate products (1996 prices)

Material	Cost per kg
Fe-9Cr steels	<$5.50 (plate form)
SiC/SiC composites	>$1000 (CVI processing) ~$200 (CVR processing of CFCs)
V-4Cr-4Ti	$200 (plate form--average between 1994-1996 US fusion program large heats and Wah Chang 1993 "large volume" cost estimate)
Nb-1Zr	~$100
Ta	$300 (sheet form)
Mo	~$80 (3 mm sheet); ~$100 for TZM
W	~$200 (2.3 mm sheet); higher cost for thin sheet

13.1.2 Overview of thermal stress capabilities of various alloys.

The key mechanical and physical properties of high-temperature refractory alloys and low-activation structural materials are summarized in Section 13.3. More detailed summaries of the properties for V-4Cr-4Ti, Fe-8-9Cr martensitic steel, SiC/SiC composites, and T-111 (Ta-8W-2Hf) are published elsewhere [1-4] and are posted on the APEX web site. A good summary of the properties for W is contained in the ITER Material Properties Handbook (pub. 4 and later versions) [5]. Figure 13.1 shows the ultimate tensile strength as a function of temperature for a several different structural materials [1,3,6-10].

The allowable stress in refractory alloys is generally controlled by the ultimate strength rather than the yield strength (due to the low work hardening capacity of refractory alloys compared to, e.g., annealed austenitic stainless steel). In addition to the ultimate strength (σ_U), the other key properties which determine the thermal stress resistance are the elastic modulus (E), Poisson's ratio (ν), thermal conductivity, (k_{th}), and mean linear coefficient of thermal expansion (α_{th}). A thermal stress figure of merit convenient for qualitative ranking of candidate high heat flux structural materials is given by $M=\sigma_U k_{th}(1-\nu)/(\alpha_{th}E)$. The maximum allowable heat flux is directly proportional to $M/\Delta x$, where Δx is the wall thickness. In addition, temperature limits (usually determined by thermal creep considerations) can be used for additional qualitative

ranking of materials. A rigorous quantitative analyses of candidate materials requires the use of advanced structural design criteria such as those outlined in section 13.2.

The mechanical properties for recrystallized refractory alloys have been used as the reference case for purposes of APEX designs. The mechanical properties of stress-relieved (non-recrystallized) refractory alloys are superior to those of recrystallized specimens, with increases in strength of up to a factor of 2 being typical. However, the possibility of stress- or radiation-enhanced recrystallization of these alloys (along with the likely inclusion of welded joints in the structure) does not allow this strength advantage to be considered for conservative design analyses.

The thermal stress figures of merit varies from ~57 kW/m for a high strength, high conductivity CuNiBe alloy at 200˚C [11] to ~2.0 for SiC/SiC at 800˚C. Cu-Ni-Be is not suitable for structural use above ~300˚C due to poor fracture toughness at elevated temperature [12], and the thermal creep strength of all copper alloys is low at temperatures above 400˚C ($0.5T_M$). Therefore, copper alloys are not attractive choices for high thermal efficiency power plants. The low thermal stress resistance of SiC/SiC is mainly due to the low thermal conductivity in currently available composites (primarily due to a combination of poor quality fibers and imprecise control of the CVI deposition chemistry). The two major classes of low-activation structural alloys, V-Cr-Ti and Fe-8-9Cr martensitic steel have figures of merit of ~6.4 (450-700˚C) and 5.4 (400˚C), respectively. The refractory alloys offer some advantage over vanadium alloys and ferritic-martensitic steel, even in the recrystallized condition. For example, pure recrystallized tungsten has a figure of merit of M=11.3 at 1000˚C, and TZM (Mo-0.5Ti-0.1Zr) has a value of M=9.6 at 1000˚C. The alloy T-111 (Ta-8W-2Hf) has the best thermal stress figure of merit among the (non-copper) alloys considered, with a value of M=12.3 at 1000˚C. Nb-1Zr has an acceptable figure of merit (M=10.1) at 600˚C, but its strength and thermal stress capability decrease at temperatures above 600˚C. Considering the high induced radioactivity of Nb compared to the other Group Vb alloys (V and Ta), the lack of a clear thermal stress performance advantage for Nb-1Zr makes this alloy less desirable for fusion energy structural applications compared to the other refractory alloys.

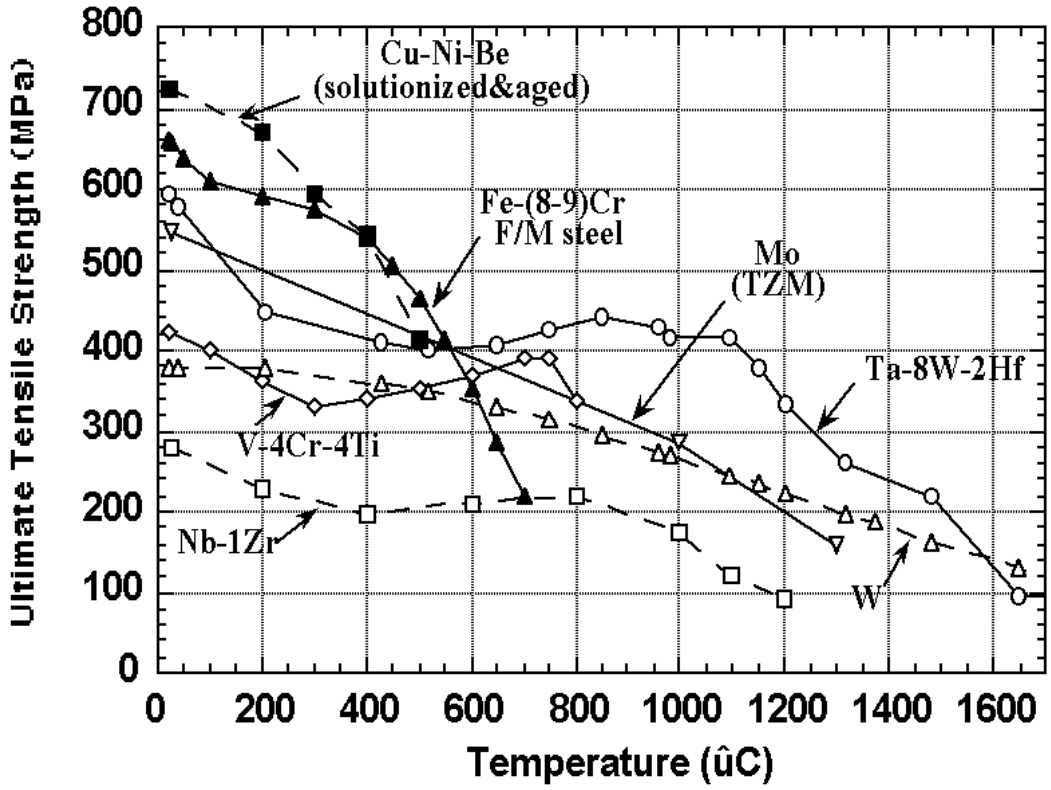

Fig. 13.1 Comparison of the ultimate tensile strength of recrystallized refractory alloys [1,6-9], solutionized and aged Cu-2Ni-0.3Be [10] and Fe-(8-9)Cr ferritic-martensitic steel [3].

13.2 Structural Design Criteria

Most advanced blanket design concepts require the first wall to operate in temperature regimes where thermal creep effects may be important. Therefore, in addition to the usual low-temperature design rules, high-temperature design rules may also have to be applied. We have adopted the ITER Structural Design Criteria (ISDC) as a basis for the design rules to be used in APEX.

13.2.1 Definitions

Some of the key definitions needed during design calculations are included here; the rest can be obtained from the Section IRB of the ISDC.

Primary stress: primary stress is defined as that portion of the total stress which is required to satisfy equilibrium with the applied loading and which does not diminish after small scale permanent deformation.

Secondary stress: secondary stress is that portion of the total stress (minus peak stresses, as defined below), which can be relaxed as a result of small scale permanent deformation. The basic characteristic of a secondary stress is that it is self-limiting.

Total stress (strain): total stress σ_{ij} (strain ε_{ij}) is the stress (strain) under the effect of all the loadings to which the component is subjected.
Membrane stress (strain): membrane stress (or strain) tensor is the tensor whose components $(\sigma_{ij})_m$ $[(\varepsilon_{ij})_m]$ are equal to the mean value of stresses σ_{ij} (ε_{ij}) through the thickness.
Bending stress (strain): the bending stress (strain) tensor is that tensor whose components $(\sigma_{ij})_b$ $[(\varepsilon_{ij})_b]$ vary linearly through the thickness and which, when integrated through the thickness, have the same bending moment as the original tensor $\sigma_{ij}(\varepsilon_{ij})$.
Peak stress: Peak stress is the increment of stress which is additive to the membrane-plus-bending stresses by reason of local discontinuities or local thermal stresses including the effects, if any, of stress concentrations.
Stress intensity: the stress intensity, $\bar{\sigma}$, at any given point is a scalar derived from the stress tensor, σ, at that point, using the following maximum shear or Tresca criterion:

$$\bar{\sigma} = \max\left(|\sigma_1 - \sigma_2|, |\sigma_2 - \sigma_3|, |\sigma_3 - \sigma_1|\right) \qquad (13.2\text{-}1)$$

where σ_1, σ_2, and σ_3 are the principal stresses.
Effective stress: the effective stress used for creep calculation is based on von-Mises effective stress, i.e.,

$$\sigma_e = \sqrt{1/2}.\left\{(\sigma_{11} - \sigma_{22})^2 + (\sigma_{22} - \sigma_{33})^2 + (\sigma_{33} - \sigma_{11})^2 + 6\left(\sigma_{12}^2 + \sigma_{23}^2 + \sigma_{31}^2\right)\right\}^{1/2} \qquad (13.2\text{-}2)$$

Stress intensity range: it is the maximum of the stress intensities of the tensor differences between the stress tensors $\sigma(t)$ and $\sigma(t')$ for every pair of times t and t' within a cycle.
Allowable primary membrane stress intensity (S_m): S_m is a temperature (T) and fluence (Φt) dependent allowable stress intensity defined as the least of the following quantities:
$\text{Min}[1/3S_{u,min}(RT, 0), 1/3S_{u,min}(T, 0), 1/3S_{u,min}(T, \Phi t), 2/3S_{y,min}(RT, 0), 2/3S_{y,min}(T, 0), 2/3S_{y,min}(T,\Phi t)]$, where $S_{y,min}$ and $S_{u,min}$ are the minimum yield and ultimate tensile strengths, respectively, and RT is room temperature.
Uniform elongation (ε_u): ε_u is defined as the plastic component of the engineering strain at the time when necking begins in a uniaxial tensile test.
True strain at rupture (ε_{tr}): ε_{tr} is defined as :

$$\varepsilon_{tr} = \ln\left(\frac{100}{100 - \%RA}\right), \qquad (13.2\text{-}3)$$

where %RA is the reduction in area (%) as determined in a uniaxial tension test at a given temperature, strain rate, and fluence.
Elastic follow-up factor (r): the r-factor provides a simplified inelastic analysis approach by which the peak inelastic strain and stress in a structure can be estimated from elastic analysis results. An r value =4 is used in ISDC as a conservative estimate for many structures made of ductile alloys with adequate strain-hardening capability. For

irradiated materials with severe loss of strain hardening capability (uniform elongation), r can be much larger.

Allowable primary plus secondary membrane stress intensity (S_e): S_e is a temperature (T) and fluence (ϕt) dependent allowable stress intensity for a material with severe loss of uniform elongation due to irradiation and is defined as follows:

$$S_e = \frac{1}{3}\left[S_{u,min}(T,\phi t) + \frac{E\alpha_1}{r_1}\left(\varepsilon_u(T,\phi t) - 0.02\right)\right] \quad \text{if } \varepsilon_u\,(T,\phi t) \bullet 2\% \qquad (13.2\text{-}4a)$$

and

$$S_e = \frac{1}{3} S_{u,min}(T,\phi t) \qquad \text{if } \varepsilon_u\,(T,\phi t) < 2\% \qquad (13.2\text{-}4b)$$

where E is Young's modulus, α_1 =0.5, and

$$r_1 = \begin{cases} \infty \text{ for } \varepsilon_u \le .02\ (2\%) \\ 4 \text{ for } \varepsilon_u > .02 \end{cases} \qquad (13.2\text{-}5)$$

Allowable total stress intensity (S_d): S_d is a temperature (T), fluence (ϕt), and r-factor dependent allowable stress intensity for total primary plus secondary stress in radiation embrittled materials, and is defined as follows:

$$S_d = \frac{2}{3}\left(S_{u,min}(T,\phi t) + \frac{E}{r}\frac{\varepsilon_{tr}(T,\phi t)}{TF}\right) \qquad (13.2\text{-}6)$$

where TF = triaxiality factor to account for the effect of hydrostatic stress on ductility,

$$TF = \frac{\sqrt{2}\,(\sigma_1 + \sigma_2 + \sigma_3)}{\left[(\sigma_1 - \sigma_2)^2 + (\sigma_2 - \sigma_3)^2 + (\sigma_3 - \sigma_1)^2\right]^{1/2}}, \qquad (13.2\text{-}7)$$

and r = elastic follow-up factor whose value is r_2 in zones of stress concentration (i.e., peak stress due to stress concentration is included), and r_3 away from zones of stress concentration.

r_2 = Max {K_T and 4} where K_T is the elastic stress concentration factor and

$$r_3 = \begin{cases} \infty \text{ for } \varepsilon_u \le .02\ (2\%) \\ 4 \text{ for } \varepsilon_u > .02 \end{cases} \qquad (13.2\text{-}8)$$

Time-dependent allowable primary stress intensity (S_t): S_t is a time and temperature-dependent allowable primary stress intensity defined as the least of the following:

(1) two thirds of the minimum stress corresponding to average creep rupture time t at temperature T,

(2) 80% of the minimum stress corresponding to time t and temperature T for onset of tertiary creep, and

(3) minimum stress to cause a creep strain of min[1%, $\varepsilon_C/5$] in time t and temperature T, where ε_C is the minimum creep ductility.

13.2.2 Design rules

Since the design studies under APEX are preliminary in nature, only elastic analysis design rules are included. For full inelastic analysis design rules, the IRB Section of the ISDC may be used. The design rules are divided into a high temperature section and a low temperature section, depending on whether thermal creep effects are or are not important. The low temperature rules are always applicable. To determine whether the high temperature rules are also to be applied, the following negligible creep test should be used.

Negligible creep test: Thermal creep is negligible over the total design lifetime of a component if the following summation limit is satisfied:

$$\sum_{i=1}^{N} \left(\frac{t_i}{t_{c_i}} \right) \leq 1 \qquad (13.2\text{-}9)$$

where the total lifetime is divided into N intervals of time; for each interval i, of duration t_i, the maximum temperature is denoted by T_i. The negligible thermal creep time t_{c_i} at a temperature T_t is calculated as the time required to accumulate a thermal creep strain of 0.05% in a uniaxial creep specimen subjected to a constant stress of 1.5 $S_m(T_t)$. If inequality (1) is satisfied, then only low temperature design rules need be applied.

13.2.2.1 Low temperature design rules

Necking and plastic instability limits
To prevent failure by necking and plastic instability, the following limits must be satisfied at all times:

$$\overline{P_m} \leq S_m(T_m, \phi t_m) \qquad (13.2\text{-}10a)$$

$$\overline{P_L + P_b} \leq K\, S_m(T_m, \phi t_m) \qquad (13.2\text{-}10b)$$

where P_m is general primary membrane stress, P_L is local primary membrane stress, P_b is primary bending stress, K is bending shape factor (= 1.5 for solid rectangular section), and S_m is evaluated at the thickness-averaged temperature (T_m) and fluence (ϕt_m).

Plastic flow localization limit
To prevent cracking due to plastic flow localization (in a material with significant loss of uniform elongation due to irradiation), the following limit must be satisfied at all times during the life of the component:

$$\overline{P_L + Q_L} \leq S_e(T_m, \phi t_m) \qquad (13.2\text{-}11)$$

where Q_L is the secondary membrane stress.

Ductility exhaustion limits
To prevent local fracture due to exhaustion of ductility (due to embrittlement), the following limits must be satisfied at all times during the life of the component:
The total stress, including peak stress, is limited by

$$\overline{P_L + P_b + Q + F} \le S_d(T, \phi t, r_2) \qquad (13.2\text{-}12a)$$

where F is peak stress (e.g., due to stress concentration), and the total stress, excluding peak stress, is limited by

$$\overline{P_L + P_b + Q} \le S_d(T, \phi t, r_3) \qquad (13.2\text{-}12b)$$

Brittle fracture limit
To prevent brittle fracture initiating from severe flaws or notches, the maximum mode I stress intensity factor, K_I, due to all primary and secondary loadings, including peak ($P_L + P_b + Q + F$), must be limited by the following:

$$K_I \le K_C(T_m, \Phi t_m) \qquad (13.2\text{-}13)$$

where K_C is the linear-elastic fracture toughness evaluated at the thickness-averaged temperature and fluence. The stress intensity factor K_I has to be determined from the analysis of a postulated surface flaw of depth a_0 , length $4a_0$, where a_0 = max [$4a_u$, h/4], a_u = largest undetectable crack length, and h = section thickness. If the full section under consideration (without the flaw) experiences plasticity, a suitable non-linear fracture parameter (e.g., J-integral) should be used instead of K.

Ratcheting limits
To prevent ratcheting due to cyclic loading, either of the following two limits should be satisfied at all times:
a) $3S_m$ limit

$$\left(\overline{P_L + P_b}\right)_{max} + \Delta\left[\overline{P} + \overline{Q}\right]_{max} \le 3S_m(T_m, \phi t_m) \qquad (13.2\text{-}14)$$

where Δ denotes range of primary (P) or secondary (Q) stress due to cyclic loading.
b) Bree-diagram limit

$$Y \le \begin{cases} \dfrac{1}{X} & \text{for } 0 \le X \le 0.5 \\ 4(1 - X) & \text{for } 0.5 < X \le 1 \end{cases} \qquad (13.2\text{-}15a)$$

where

$$X = \frac{\overline{P_m}}{S_y} \quad \text{or} \quad X = \frac{\overline{P_L + \frac{P_b}{K}}}{S_y} \text{ and } Y = \frac{\Delta\left[\overline{P} + \overline{Q}\right]}{S_y}, \qquad (13.2\text{-}15b)$$

and the yield stress S_y is evaluated at the average of the thickness-averaged temperatures at the "cold" and "hot" ends of the cycle.

Fatigue limit
To prevent the initiation of a fatigue crack due to cyclic loading, the fatigue usage fraction V at the end of life must satisfy the following limit

$$V = \sum_{j=1}^{J} \frac{n_j}{N_j\left(\overline{\Delta\varepsilon}_j\right)} < 1 \qquad (13.2\text{-}16)$$

where the lifetime is divided into J type of cycles. For each cycle type j, characterized by n_j cycles at an equivalent strain range $\overline{\Delta\varepsilon}_j$ and average temperature T_j during the cycle, N_j is the allowable cycles. If $\overline{\Delta\varepsilon}_j$ is calculated elastically, it should be corrected for possible plasticity effects (e.g., by Neuber's rule for notches).

13.2.2.2 High temperature design rules

Creep damage limits
To guard against creep damage, the following limits must be satisfied:

$$\overline{P_m} \leq S_t(T_m, t) \qquad (13.2\text{-}17a)$$

$$\overline{P_L + P_b / K_t} \leq S_t(T_m, t) \qquad (13.2\text{-}17b)$$

where t is the design lifetime, and $K_t = (K+1)/2$. If the lifetime involves variable stress and temperature history, these equations should be replaced by limits on usage fraction sums.

Creep-ratcheting limit
If the negligible creep test (Eq. 13.2-9) is not satisfied, then in addition to satisfying the low temperature ratcheting limit based on Bree diagram (Eq. 13.2-15a), the high temperature ratcheting limit should be satisfied by first calculating an effective core stress σ_c for creep calculations as follows:

$$\sigma_c = Z s_{yL} \qquad (13.2\text{-}18)$$

where S_{yL} is the S_y value at the "low" temperature extreme of the cycle and Z is a creep stress parameter defined in terms of X and Y (which are defined in Eq. 13.2-15b),

$$Z = X \text{ for } X+Y \leq 1 \qquad (13.2\text{-}19a)$$

$$Z = Y + 1 - 2\sqrt{(1-X)Y} \text{ for } 1-X \leq Y < 1/(1-X) \qquad (13.2\text{-}19b)$$

$$Z = XY \text{ for } Y > 1/(1-X) \qquad (13.2\text{-}19c)$$

The total creep strain accumulated during the lifetime due to a stress $1.25\sigma_C$ should be less than min[1%, $\varepsilon_C/5$] where ε_C is the minimum creep ductility during the cycle. If the lifetime involves more than one types of cycles of stress and temperature, the criterion is satisfied by the use of usage fraction sums.

Creep-fatigue limit
If the negligible creep test (Eq. 13.2-9) is not satisfied, then creep damage (W) has to be added to the fatigue damage (V) as evaluated in Eq. 13.2-16, i.e.,

$$V+W < 1 \qquad (13.2\text{-}20)$$

where W is the creep damage obtained by first dividing the lifetime into K intervals. Each interval k of duration Δt_k is characterized by a maximum temperature T_k, a maximum effective stress $\sigma_{e,k}$. The following sum defines the creep damage W:

$$W = \sum_k \frac{\Delta t_k}{t_{R,k}} \qquad (13.2\text{-}21)$$

where $t_{R,k}$ is the minimum time to creep rupture at temperature T_k and stress $1.25\sigma_{C,k}$.

13.3 Summary of thermophysical properties (unirradiated and irradiated)

Tables 13.2-13.6 provide analytical expressions for the temperature-dependent mechanical and thermophysical properties for five of the structural materials considered for APEX. The analytical expressions were determined from least-squares fits of experimental data. Further details are available at the APEX web site and in references [1-5].

Table 13.2. Summary of V-4Cr-4Ti Properties [1,2].

Ultimate Tensile Strength (unirradiated)
σ_{UTS}(MPa)= 446 - 0.806*T + 0.00221*T^2 - 1.79e-06*T^3 + 1.82e-10*T^4 (T in ˚C)

Yield Strength (unirradiated)
σ_Y(MPa)= 377 - 0.704*T + 0.00090*T^2 - 1.23e-07*T^3 - 1.98e-10*T^4 (T in ˚C)

Elongation
e_{tot} , RA are high in unirradiated and irradiated conditions
e_u is high in unirradiated conditions, moderate (>2%) after irradiation at T>430˚C
and low (<1%) for irradiation at T<400˚C

Elastic constants
E_Y (GPa) =128 - 0.00961*T (T in Kelvin)
G (GPa) =48.8 - 0.00843 *T (T in Kelvin) $\nu=(E_Y/2G) - 1$

Thermophysical properties
α_{th} = 9.03767 + 0.00301422*T + 4.95937x10^{-7} * T^2 ppm/˚C (T in ˚C)
C_P = 0.5755 - 21.1 / T J/g-K (T in Kelvin)
k_{th} = 27.8 + 0.0086 T W/m-K (T in Kelvin)

Recommended operating temperature limits (structural applications)
Tmin = 400˚C (due to rad.-induced increase in DBTT at low T_{irr})
Tmax = 700˚C (corrosion/chemical compatibility and thermal creep)

Table 13.3. Summary of 8-9Cr Ferritic/Martensitic Steel Properties [3].

Ultimate Tensile Strength (unirradiated)
σ_{UTS}(MPa)= 683 - 1.162*T + 0.00547*T^2 - 1.17e-05*T^3 + 6.24e-09*T^4 (T in ˚C)

Yield Strength (unirradiated)
σ_Y(MPa)= 531 - 0.388*T + 0.00148*T^2 - 2.40e-06*T^3 - 1.45e-10*T^4 (T in ˚C)

Elongation
e_{tot} , RA are moderate to high in unirradiated and irradiated conditions (e_{tot}~8-10% for T_{irr}<400˚C)
e_u is low in unirradiated (0.2-7%) and irradiated (<3%) conditions

Elastic constants
E_Y (GPa) =233 - 0.0558*T 20- 450˚C (T in Kelvin)
G (GPa) =90.1 - 0.0209 *T 20- 450˚C (T in Kelvin) $\nu=(E_Y/2G) - 1$

Thermophysical properties
α_{th} = 10.4 ppm/˚C (20˚C) to 12.4 ppm/˚C (700˚C)
C_P = 0.47 J/g-K (20˚C) to 0.81 J/g-K (700˚C)
k_{th} = 33 W/m-K (20-700˚C)

Recommended operating temperature limits (structural applications)
Tmin = 250˚C (due to rad.-induced increase in DBTT at low T_{irr})
Tmax = 550˚C (thermal creep); Tmax~700˚C for oxide dispersion strengthened steels?

Table 13.4. Summary of SiC/SiC Properties [4].

Ultimate Tensile Strength (unirradiated)
σ_{UTS} ~ 220-240 MPa (20-1000˚C)

Proportional Limit Strength (unirradiated)
σ_Y~70 MPa (20-1000˚C)

Elongation
e_{tot} , eu, RA are very low in unirradiated and irradiated conditions

Elastic constants
E_Y GPa) ~400 GPa 20- 1000˚C (Sylramic or Hi-Nicalon type S fibers, 10% matrix porosity)
G (GPa) =~165 GPa 20- 1000˚C
ν=0.16 20- 1000˚C

Thermophysical properties
α_{th} ~ 2.5 ppm/˚C (20˚C) to 4.5 ppm/˚C (1000˚C)
C_P = 1110 + 0.15 T - 425 $e^{-0.003T}$ J/kg-K (1000˚C)
k_{th} = 10-15 W/m-K (400-1000˚C, after irradiation)

Recommended operating temperature limits (structural applications)
Tmin ~ 500˚C? (due to rad.-induced decrease in thermal conductivity)
Tmax = 1000˚C? (due to cavity swelling)

Table 13.5. Summary of recrystallized Ta-8W-2Hf (T-111) properties.

Ultimate Tensile Strength (unirradiated)
σ_{UTS}(MPa)=630 - 1.532*T +0.003388*T^2 -2.807e-06*T^3 +7.338e-10*T^4 (T in ˚C)

Yield Strength (unirradiated)
σ_Y(MPa)= 612 - 1.743*T +0.003585*T^2 -3.076e-06*T^3 +8.819e-10*T^4 (T in ˚C)

Elongation
e_{tot} , RA are high in unirradiated and irradiated conditions
e_u is high in unirradiated conditions, moderate (>2%) after irradiation at T>650˚C and low (<1%) for irradiation at T<600˚C

Elastic constants (pure Ta)
E_Y (GPa) =169 - 0.00822*T - 1.66x10^{-6} T^2 (T in Kelvin)
G (GPa) =77.4 - 0.0173 *T (T in Kelvin) $\nu=(E_Y/2G) - 1$
ν=0.35 (300 K)

Thermophysical properties
α_{th} = 5.9 ppm/˚C (20˚C) and 7.6 ppm/˚C (1650˚C)
C_P = 150 J/kg-K (20˚C)
K_{th} (W/m-K)=41.0 + 0.020 T - 6.32x10^{-6} T^2 (T in ˚C)

Recommended operating temperature limits (structural applications)
Tmin = 650˚C (due to radiation-induced increase in DBTT at low T_{irr})
Tmax = 1200˚C (thermal creep)

Table 13.6. Summary of recrystallized W-(5-10%) Re properties. The tensile properties and coefficient of thermal expansion and specific heat are based on pure recrystallized tungsten data.

Ultimate Tensile Strength (unirradiated)
σ_{UTS}(MPa)=377.9 + 0.03207*T - 1.955x10^{-4}*T^2 + 5.13x10^{-8}*T^3 (T in ˚C)

Yield Strength (unirradiated)
σ_Y(MPa)= 94.2 - 0.0214*T -2.12x10^{-6}*T^2 -7.48x10^{-10}*T^3 (T in ˚C)

Elongation
e_{tot}(%)=20.8 + 0.053*T-2.18x10^{-5}*T^2 (T>500˚C)

Elastic constants
E_Y (GPa) =398 - 0.00231*T - 2.72x10^{-5} T^2 (T in •C) --pure W
ν=0.279 + 1.09x10^{-5} T (T in •C)
W-25Re: ν(20•C)=0.30, E(20•C)=410 GPa, G(20•C)=159 GPa

Thermophysical properties
α_m (10^{-6}/•C)= 3.9 + 5.8x10^{-5}*T + 5.7x10^{-11}*T^2 - 2.0x10^{-14}*T^3 (T in ˚C)
C_P (J/kg-K) = 128+ 0.033*T - 3.4x10^{-6}*T^2 (T in ˚C)
K_{th} (W/m-K)~85 W/m-K (1000-2400˚C) --conductivity decreases with increasing Re content

Recommended operating temperature limits (structural applications)
Tmin = 900˚C (due to radiation-induced increase in DBTT at low T_{irr})
Tmax = 1400˚C (Li, Pb-Li corrosion/chemical compatibility and thermal creep)

13.3.1. Overview of Radiation Effects in Refractory Metals

Void swelling is not anticipated to be a lifetime-limiting issue due to the body-centered cubic (BCC) structure of the high-temperature refractory alloys. The existing fission reactor data base (e.g., [13]) indicates moderate swelling (<2%) for doses up to 10 dpa or higher. The effects of fusion-relevant He generation on swelling in these alloys is uncertain. The potential void swelling regimes are ~600 to 1000˚C for all 4 types of refractory alloys (Mo, W, V, Ta) considered for APEX. Radiation-enhanced recrystallization (potentially important for stress-relieved Mo and W alloys) and radiation creep effects need to be investigated.

Radiation hardening can lead to a large increase in the ductile to brittle transition temperature of BCC alloys [14]. The radiation hardening in BCC alloys at low temperatures (<0.3 T_M) is typically pronounced even for doses of ~1 dpa [15-18]. The amount of radiation hardening typically decreases rapidly with irradiation temperature above 0.3T_M, and radiation-induced increases in the DBTT may be anticipated to be acceptable at temperatures above ~0.3 T_M (although experimental verification is needed,

particularly for the Mo, W and Ta alloys). Unfortunately, there are very few studies on the mechanical properties of high temperature refractory alloys irradiated and tested at temperatures above 0.3 T_M (~800˚C for Mo and W alloys). There are no known fracture toughness measurements on high temperature refractory alloys (Mo, W, Ta alloys) following neutron irradiation at any dose or temperature. The Charpy impact database on irradiated high temperature refractory alloys is also virtually nonexistent.

In general, the Group Vb alloys (V, Nb, Ta) exhibit better ductility before and after irradiation compared to Group VI (Mo and W) alloys. The existing mechanical properties data base is very limited for irradiated Nb and Ta alloys (e.g., [13]). Some qualitative trends for Nb and Ta alloys can be inferred from the larger database [18] on irradiated V alloys. A moderate mechanical properties data base exists for irradiated Mo alloys (although most of the data were obtained at relatively low irradiation temperatures). Very little information is available on the effect of irradiation on the tensile properties of tungsten and W alloys.

The following paragraphs summarize the Ta, Mo and W alloy radiation hardening database. These data were used to make rough estimates of the minimum allowable operating temperature of structural alloys due to radiation embrittlement concerns. A Ludwig-Davidenkov relationship was used to estimate the ductile to brittle transition temperature; brittle behavior occurs when the temperature dependent stress exceeds the cleavage stress. Due to the lack of controlled fracture mechanics data on irradiated specimens, the derived estimates of the minimum allowable operating temperature have relatively high uncertainty (±100-200˚C). Operation at lower temperatures may be allowed for very low stress designs.

13.3.1.1 Ta Alloys: T-111 (Ta-8W-2Hf)

Significant radiation hardening has been observed in Ta-(8-10%)W alloys irradiated at 415 and 640˚C (σ_y, UTS>1000 MPa) to a fluence of 1.9×10^{26} n/m^2, E>0.1 MeV, whereas very little hardening occurred at an irradiation temperature of 800˚C [13]. This neutron fluence corresponds to a damage level of 2.5 dpa in Ta (10 dpa in steel). Since the matrix hardening at 415 and 640˚C is well above the level which produces brittle behavior in other BCC metals such as V alloys [18], it is assumed that the Ta alloy is embrittled at these irradiation conditions (the Charpy impact or fracture toughness data needed to confirm this are not available). Therefore, the estimated minimum operating temperature for Ta-(8-10%)W alloys is estimated to be ~700˚C, based on DBTT considerations

13.3.1.2 Mo Alloys (TZM, Mo-Re)

Pronounced radiation hardening occurs in Mo and Mo alloys such as TZM and Mo-Re up to ~700˚C. For example, the tensile strength of Mo-5%Re after irradiation at 800˚C to a dose of 11 dpa was ~1000 MPa for a test temperature of 400˚C [19,20]. Very low tensile elongations were observed in Mo, TZM, Mo-Re, and Mo-Zr-B alloys for irradiation and test temperatures up to 700-800˚C and damage levels of 5-20 dpa [19,21-

23]. Irradiation data at doses >0.1 dpa are not yet available for the recently-developed Mo-TiC alloys which have been reported to have improved ductility compared to conventional Mo alloys both before and after low dose irradiation [24]. It is important to note that the impact studies carried out to date on these fine-grained Mo-TiC alloys have used smooth (un-notched) specimens; it is difficult to produce a quantitative assessment of the fracture resistance without a stress concentrator. The estimated minimum operating temperature for Mo alloys is assumed to be ~800˚C, based on the limited tensile data. Further mechanical properties data on Mo alloys at irradiation and test temperatures of 650-950˚C are needed to develop a better estimate of the minimum operating temperature associated with DBTT effects.

13.3.1.3 W and W Alloys

Very little information is available on the mechanical properties of irradiated W alloys. Tensile elongations of ~0 have been obtained for W irradiated at relatively low temperatures of 400 and 500˚C (0.18-0.21 TM) and fluences of $0.5\text{-}1.5\text{x}10^{26}$ n/m^2 (<2 dpa in tungsten) [13,21,25]. Severe embrittlement (DBTT>900˚C) was observed in un-notched bend bars of W and W-10%Re irradiated at 300˚C to a fluence of $0.5\text{x}10^{26}$ n/m^2 (~1 dpa) [26]. The rate of embrittlement was found to be most rapid in the W-10%Re alloy. Irradiation data are not yet available for the recently developed fine-grained W-TiC alloy [27] which has been reported to have improved ductility compared to existing W alloys. Since mechanical properties data are not available for tungsten or W alloys irradiated at high temperatures, an accurate estimate of the DBTT vs. irradiation temperature cannot be made. The minimum operating temperature which avoids severe radiation embrittlement is expected to be 800-1000˚C, scaling from the limited Mo alloy data base. Additional data on tungsten and W alloys irradiated at 700-1000˚C are clearly needed before a more accurate estimate can be made.

13.4 Coolant/structure chemical compatibility

13.4.1 Temperature and Oxygen Partial Pressure Limits for Mo and W Alloys.

At low temperatures and pressures, the chemical reactions of a gas with a solid generally result in the formation of solid corrosion products. However, at elevated temperatures and low oxygen partial pressures, the formation of volatile corrosion products is thermodynamically favored. The chemical compatibility issues are examined based on thermodynamic and non-equilibrium analysis to estimate upper bounds for operating temperatures and oxygen partial pressures in the He-coolant.

The approach to model the high-temperature oxidation is to use a quasi-equilibrium treatment of heterogeneous reactions for the systems oxygen-W and oxygen-Mo. The rate-limiting step in these reactions is the trapping (adsorption) of oxygen atoms until equilibrium is reached. Assuming that the helium pressure is P_{sys} and the gas temperature is T*, the oxygen partial pressure (P_{O2}) is given by:

$$P_{O_2,} = appm \times 10^{-6} P_{sys} \qquad (13.4\text{-}1)$$

The adsorption of oxygen depends on the oxygen impingement (Z_{O2}) per unit area of wall surface, given by:

$$Z_{O_2} = P_{O_2}\sqrt{2\pi M_{O_2} RT} \tag{13.4-2}$$

were M_{O2} is the molar weight of oxygen, R is the universal gas constant and T is in K. For W, the thermodynamic reactions take place based on:

$$x\,W(s) + \frac{1}{2} y\,O_2(g) \Leftrightarrow W_x O_y(g) \tag{13.4-3}$$

A similar reaction describes the oxidation of Mo, however, at temperatures between 1500 and 2500K the reaction is more precisely described by:

$$Mo(s) + \frac{1}{2}(3-\alpha)\,O_2(g) \Leftrightarrow Mo\,O_2(g) + (1-\alpha)\,Mo\,O_3(g) \tag{13.4-4}$$

The formation enthalpies and entropies of the oxides of Mo and W are given in Table 13.7. The quasi-equilibrium treatment of oxidation is based on the method developed by Batty and Stickney [28]. The principal parameter in the quasi-equilibrium treatment is the equilibration probability, ζ, which depends on the probability of the impinging molecules to have sufficient energy to surmount the activation barrier. If ζ_{O2} represents the probability that an impinging molecule will be equilibrated, then the rate of adsorption or equilibration Γ_{O2} is:

$$\Gamma_{O_2'} = \zeta_{O_2} Z_{O_2'} \tag{13.4-5}$$

were Z_{O2} is the impingement rate of O_2 molecules on the surface given by equation (2). Letting *i* be W_xO_y and the Gibbs Free energy be:

$$\Delta G_i(T) = \Delta H_i(T) - T\Delta S_i(T) \tag{13.4-6}$$

the following system of equations can be solved for the partial pressure of oxygen, which results in the equilibration of the impinging oxygen molecules on the wall:

$$\begin{aligned} K_i &= \frac{P_i}{(P_{O_2})^{y/2}} = \exp(-\Delta G_i(T)/RT) \qquad \text{i = 1,2,..., N} \\ \mathrm{P_O} &= \sqrt{P_{O_2}}\exp(-\Delta G_O/RT) \\ P_{O_2'} &= P_{O_2} + P_O + \sum_1^N P_i \end{aligned} \tag{13.4-7}$$

The equilibration probabilities have been established for W:

$$\zeta_{O_2} = \exp[10.3498 - \frac{2.7607\times 10^4}{T}] \tag{13.4-8}$$

and for Mo:

$$\zeta_{O_2} = 3.2\times 10^4 \times 10^{-1.186\times 10^4/T} \tag{13.4-9}$$

were T is in K.

Mass-spectrometric investigations of gas-solid chemical reactions resulting in the formation of volatile W-oxides and Mo-oxides can be found in references [29-32] and [33-35], for W and Mo, respectively. An example of evaporation rate measurements for W-oxides [29] is shown in Fig. 13.2. All measurements show a distinct maximum for W at around 2200 K. The set of equations given above have been solved to determine the

erosion rate by volatile oxidation for the W and Mo system. Estimates for the evaporation rate of W and Mo under typical APEX operating conditions (10 MPa helium; 1ppm oxygen) are shown in Fig. 13.3. Similar to the measurements the W evaporation rate also reaches a maximum value at 2200 K and that of Mo reaches an asymptotic maximum around the same temperature. However, the estimated rates of evaporations are well above any experimental findings. The reason for the higher predicted evaporation rates is that the boundary layer effects on inhibition of the evaporated oxides in a moving coolant are not reflected in the above model.

Table 13.7: Enthalpies and Entropies for W and Mo.

Tungsten		**Molybdenum**		
Species	**$\Delta Hf_{298.15}$ (kcal/g.mole)**	**Species**	**$\Delta Hf_{298.15}$ (kcal/g.mole)**	**$\Delta Sf_{298.15}$ (cal/g.mole.K)**
O(g)	59.559	O(g)	61.3	16
W O(g)	101.6	Mo O(g)	95	25.5
WO_2 (g)	18.3	MoO_2 (g)	11.0	9.0
W O_3 (g)	-70.0	Mo O_3 (g)	-80	-15.5
W_2 O_6 (g)	-278.2	Mo_2 O_6 (g)	-270	-72
W_3O_8 (g)	-408.7	Mo_3O_8 (g)	-400	-118
W_3O_9 (g)	-483.6	Mo_3O_9 (g)	-463	-132
W_4O_{12} (g)	-670.2	Mo_4O_{12} (g)	-640	-190

13.4.1.1 Boundary layer effects

Under laminar flow conditions, the oxygen impingement rate can be significantly lower compared with a static coolant. The reason is the formation of a boundary layer, which adds resistance for the impinging oxygen. To estimate the effects of the boundary layer the collisional and the boundary layer resistances have to be estimated. The kinetic or collisional impingement rate has to balance the boundary layer diffusion rate. This condition allows the formulation of a "blowing" factor or the reduction in oxygen impingement rate because of the existence of the laminar boundary. The following set of equations provide the boundary layer resistance (R_B) term:

$$R_B \cong \frac{P_t}{\rho_g V St_m f_b}$$

$$St_m = 0.0296\,\mathrm{Re}^{-0.2}\,Sc_i^{-0.4} \qquad (13.4\text{-}10)$$

$$Sc_i = 0.145 M_i^{0.556}$$

where St_m is the Stanton number and Sc_i is the Schmidt number.

The kinetic resistance (R_k)term is given by:

$$R_{Ki} = \sqrt{\frac{2\pi R T_S}{M_i}} \tag{13.4-11}$$

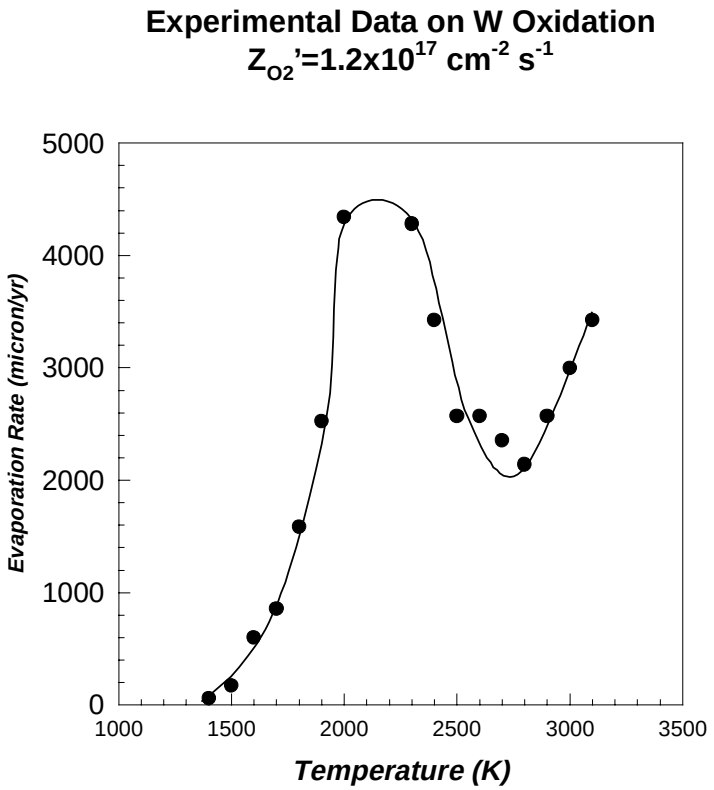

Figure 13.2: Experimental evaporation rates for W exposed to oxygen partial pressure of 300 torr after reference [29].

Using the boundary layer and the collisional resistances the surface recession (X) rate is determined as:

$$\left(\frac{dX}{dt}\right)_{Boundary} = \frac{(dX/dt)_{Kinetic}}{1 + R_B/R_k} \tag{13.4-12}$$

The results of applying the effects of the boundary resistance to the recession rate of W and Mo are shown in Figure 13.4.

The effect of a boundary layer resistance to the oxygen impingement rate and the inhibition of the evaporated oxides of W and Mo can result in several orders of

magnitude reduction of evaporation rates. The above model does not take into account many of the physical features of real wall-coolant interactions, such as, roughness, bends, and temperature variations along the flow. These issues will affect the final evaporation rate, however it is reasonable to assume that the evaporation rate of W and Mo will be below a few microns per year, when operated in a temperature range between 1200 and 1300^{o}C.

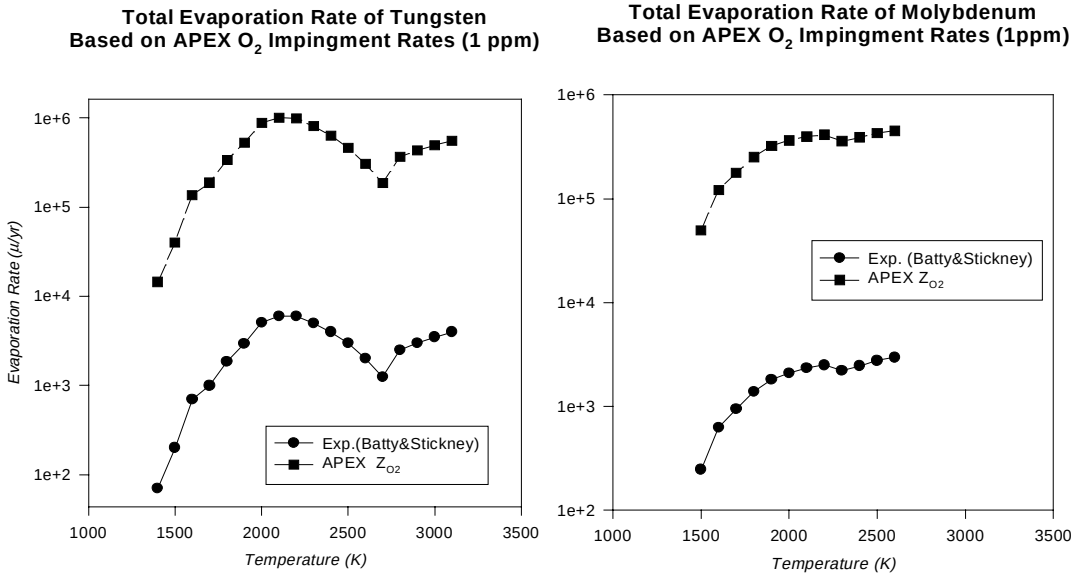

Figure 13.3: Model prediction of W and Mo evaporation rates based on 10 MPa He-coolant containing 1 ppm oxygen.

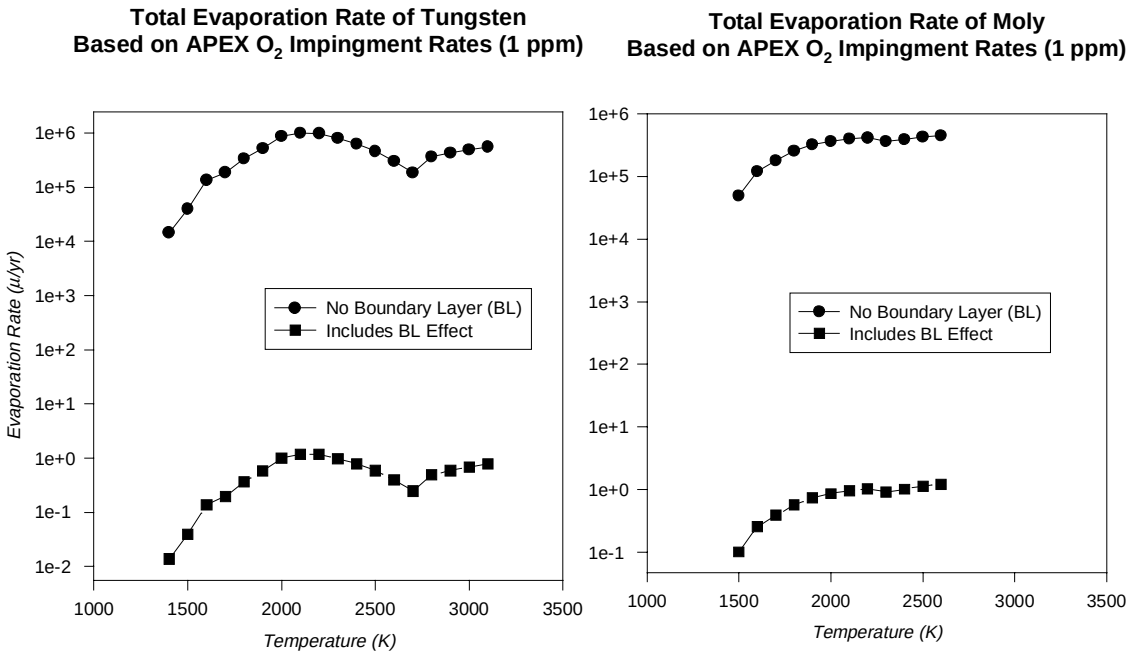

Figure 13.4: Boundary layer effect model of W and Mo evaporation rates based on 10 MPa He-coolant containing 1 ppm oxygen.

In summary, formation of volatile oxides can lead to pronounced surface erosion of Group VI metals (Mo, W) at elevated temperatures. The evaporation rate increases rapidly up to ~2000K in both Mo and W. If boundary layer scattering effects are ignored, the evaporation rate exceeds 100 μm/y at ~1500 K in both materials for 1 ppm oxygen in He at a pressure of 10 MPa. Boundary layer effects may reduce the evaporation rate by several orders of magnitude. The calculations suggest that limitations on mass transport through the boundary layer may reduce the erosion rate to less than 10 μm/y at wall temperatures up to 2600 K in both Mo and W.

13.4.2 Temperature and Oxygen Partial Pressure Limits for V, Nb and Ta Alloys.

In contrast to the oxidation (corrosion) concerns present in the Group VI metals (Mo, W), the main concern with oxygen in the Group V metals (V, Nb, Ta) is oxygen ingress. Oxygen pickup in the Group V metals causes matrix hardening, which in turn produces an increase in the ductile-to-brittle transition temperature (DBTT). For example, the matrix oxygen concentration must be below ~1500 ppm to keep Charpy DBTT below room temperature in vanadium (cf. Fig. 13.5). All of the Group V metals have high affinity for oxygen. For example, the oxygen solubility limit in vanadium is ~1-3 wt.% at T=20-900˚C. Therefore, extremely low oxygen partial pressures are required to prevent oxygen pickup based on thermodynamic considerations alone. The vanadium/vanadium oxide solvus occurs at 10^{-47} atm for T=525˚C and at 10^{-36} atm at T=725˚C ([36].

In practice, the matrix oxygen contents can be significantly lower than these thermal equilibrium values due to two effects: Formation of a protective surface oxide film or limiting the oxygen partial pressure in the surrounding atmosphere. The existence of a protective surface oxide film at low temperatures can limit the ingress of oxygen (logarithmic oxide film growth at very low temperatures; parabolic growth at moderate temperatures, >400˚C in vanadium). However, linear (rapid) oxygen pickup occurs at high temperatures in the Group V metals [6]. Therefore, formation of a protective oxide film is not effective at preventing oxygen pickup at the elevated temperatures where these metals would be expected to operate in fusion reactors.

The kinetics for oxygen pickup in vanadium alloys at moderate to high oxygen partial pressures is controlled by the protective oxide growth rate. However, a high oxygen content (sufficient for embrittlement) exists at depths well beyond the oxide scale layer [40]. The V-4Cr-4Ti activation energy for oxygen diffusion is ~130 kJ/mol [41], whereas V-4Cr-4Ti oxide growth has an activation energy of ~180-200 kJ/mol [42]. For an exposure time of 10^4 h (420 days) at 700˚C, the calculated oxide thickness for V-4Cr-4Ti would be only ~0.4 mm (assuming parabolic kinetics) whereas the calculated oxygen diffusion depth would be nearly 4 mm. The corresponding oxygen diffusion depth for exposure at 600˚C is 1.6 mm.

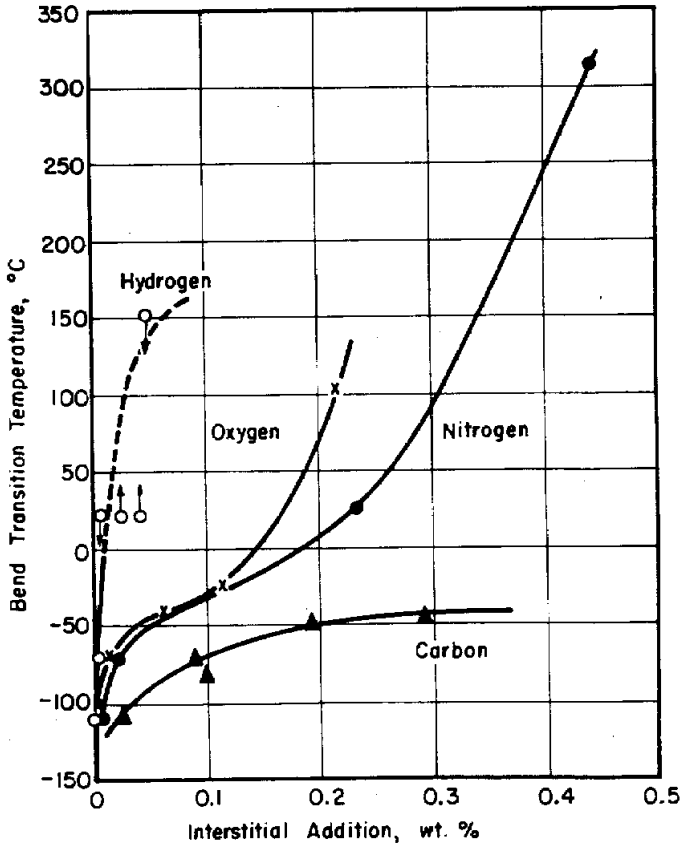

Fig. 13.5. Effect of interstitial solute additions on the (un-notched) bend transition temperature of vanadium [6], based on data from Loomis and Carlson [37]. Similar embrittlement behavior has also been observed for V-4Cr-4Ti alloys (e.g., [38,39])

Therefore, the only feasible method to prevent unacceptable oxygen pickup in Group V (vanadium and tantalum) alloys from non-lithium coolants at high temperatures is to limit the oxygen partial pressure. The oxygen impingement flux is $J_O=P_O(2\pi m_O RT)^{1/2}$, assuming an equilibration constant of unity. Creation of a monolayer of chemisorbed oxygen on Group V metals at T>400˚C requires~1 Langmuir exposure (10^{-6} torr-s).

The oxygen pressure limits for Group V metals in Table 13.8 were obtained using the assumptions that subsurface incorporation of the chemisorbed oxygen and matrix oxygen diffusion are not rate-limiting steps (valid for high temperatures and low p_O levels). Additional assumptions were: planar geometry, 3 mm slab thickness, and oxygen ingress from one side only.

Table 13.8. Summary of the exposure time needed to pick up 100-1000 ppm oxygen.

	Exposure time to achieve listed oxygen content	
Oxygen partial pressure	100 wt.ppm O	1000 wt.ppm O
10^{-8} torr	94 h	940 h
10^{-10} torr	9400 h	94,000 h (11 yr)

In conclusion, oxygen partial pressures below 10^{-11} torr would certainly be sufficient to keep oxygen pickup to acceptably low levels in Group V metals for expected structural material lifetimes (10 to 50 years). Oxygen partial pressures of ~10^{-10} torr may also be tolerable. Boundary layer effects have not been considered in this simple calculation. This may allow even higher oxygen partial pressures to be present without causing embrittlement due to oxygen pickup.

13.4.3 Review of Corrosion Database for Li, Pb-Li, Sn-Li, and Flibe -coolant Concepts.

The chemical compatibility of low activation and refractory structural alloys with liquid metals and Flibe is summarized in Table 13.9. In general, the refractory alloys have very good compatibility with the liquid metals and salts of interest for fusion applications. Corrosion associated with impurities in the coolant is one of the key engineering issues for fusion applications.

The Li chemical compatibility data base for high temperature refractory alloys can be summarized as follows: The alloy T-111 (Ta-8W-2Hf) has good compatibility with lithium for exposure temperatures up to 1370˚C (both static and circulating loop experiments). Similarly, the existing corrosion data for Nb-1Zr exposed to lithium indicates good compatibility up to 1000˚C (static and circulating loops). Pure tungsten and W alloys are generally compatible with lithium up to 1370˚C (attack observed at $\geq$1540˚C). Mo alloys (TZM) also have good compatibility with lithium up to 1370˚C (attack observed at $\geq$1540˚C).

Table 13.9. Maximum temperatures of structural alloys (bare walls) in contact with high-purity liquid coolants, based on a 5 μm/yr corrosion limit

	Li	Pb-17 Li	Flibe
F/M steel	550-600°C [43-46]	450°C [43,44,46,47]	700°C ? 304/316 st. steel [48,49]
V alloy	600-700°C [43,50,51]	~650°C [43,52]	?
Nb alloy	~1300°C [53-55]	>600°C [52] (>1000°C in Pb) [56]	>800°C [57]
Ta alloy	>1370°C [53,54]	>600°C [52] (>1000°C in Pb) [56]	?
Mo	>1370°C [53,54,58]	>600°C [52] (<1000°C in Pb) [56]	>1100°C? [59,60]
W	>1370°C [53,54]	>600°C [52]	>900°C in LiF [60]
SiC	~550°C ? [61,62]	>800°C ? [[62,63]	?

The chemical compatibility data base for Flibe is much less certain compared to the other candidate liquid breeder coolants. The limited data suggest that Flibe has good compatibility with several of the proposed structural metals, but data are not yet available for many of the candidate structural materials.

The limited experimental database on corrosion of structural materials in Sn (static tests only) is summarized below. This information is relevant for the evaluation of Sn-Li as a potential coolant/breeding material. Austenitic and ferritic steels corrode rapidly in Sn at temperature above ~400°C. Additional experimental data are needed for other structural materials, although several materials appear to be compatible with Sn at temperatures of interest for APEX. The physical nature of the Sn interaction with structural materials needs to be experimentally examined, so as to plan for corrosion control strategies.

Nb: no corrosion observed at ~600˚C
chemical attack occurred at 800˚C [64] and 1000˚C [56,65]

Ta: chemical attack observed at both 600-630 [64,66] and 800˚C [64]
intergranular penetration observed at 1000˚C [56,65,67]

Mo: minimal corrosion observed below ~600˚C [66]
chemical attack observed at both 630 and 800˚C [64]
significant corrosion (predominantly intergranular) observed at 1000˚C [56,65-68]
-1.7% weight loss after 340 h at 1000˚C [66,68]

W: good chemical resistance at 630˚C; moderate attack at 800˚C [64]
Very little corrosion (10 ppm weight loss) observed after 40 h at 1000˚C [68]

moderate corrosion (<5 μm) observed after 100 h at 1000˚C [56]

Austenitic, Ferritic stainless steels: rapid attack at temperatures above 400-500˚C [69-71]

SiC: "no interactions detected" for SiC exposed to Sn-Pb-Bi mixture at 760˚C [63]

13.5 Summary and conclusions

The determination of minimum and maximum allowable temperature limits for structural materials requires consideration of several processes. In BCC alloys, the minimum operating temperature limit will likely be determined by radiation hardening and embrittlement issues. The minimum temperature limit for SiC/SiC composites will likely be determined by thermal conductivity degradation effects (the amount of thermal conductivity degradation in SiC is particularly pronounced at lower irradiation temperatures). The upper temperature limit for BCC alloys will typically be determined by either thermal creep, helium embrittlement, or chemical compatibility issues. The upper temperature limit for SiC/SiC will likely be determined by either void swelling or chemical compatibility issues (helium embrittlement and thermal creep would be expected to become pronounced at higher temperatures than the void swelling limit is SiC, which is estimated to occur at ~1000˚C).

Figure 13.6 summarizes the operating temperature windows (based on thermal creep and radiation damage considerations) for some of the structural materials considered for APEX. Additional temperature restrictions associated with coolant compatibility issues are summarized in section 13.4. The lower temperature limits in Fig. 13.6 for the refractory alloys and ferritic/martensitic steel are based on fracture toughness embrittlement associated with low temperature neutron irradiation. An arbitrary fracture toughness limit of ~30 MPa-$m^{1/2}$ was used as the criterion for radiation embrittlement. Further work is needed to determine the minimum operating temperature limit for oxide dispersion strengthened (ODS) ferritic steel. The assumed value of 300˚C used in Fig. 13.6 for ODS ferritic steel was based on results for HT-9 (Fe-12Cr ferritic steel). The minimum operating temperature for SiC/SiC is based on radiation-induced thermal conductivity degradation, whereas the minimum temperature limit for CuNiBe was simply chosen to be near room temperature. Low temperature radiation embrittlement is not sufficiently severe to preclude using copper alloys near room temperature, although there will be a significant reduction in strain hardening capacity as measured by the uniform elongation in a tensile test. The high temperature limit was based on thermal creep for all of the materials except SiC and CuNiBe. A Stage II creep deformation limit of 1% in 1000 h ($3x10^{-9}$ s^{-1} steady-state creep rate) for an applied stress of 150 MPa was used as an arbitrary criterion for determining the upper temperature limit associated with thermal creep. Further creep data are needed to establish the temperature limits for longer times and lower stresses in several of the candidate materials. Helium embrittlement of grain boundaries may cause a further reduction in the upper temperature limit, but sufficient data under fusion-relevant conditions are not available for any of the candidate materials. The high temperature limit for SiC was determined by void swelling

considerations and the limit for CuNiBe was associated with its low unirradiated fracture toughness at elevated temperatures.

With the exception of CuNiBe, the temperature windows summarized in Fig. 13.6 are sufficiently wide (ΔT=300-400˚C) to enable attractive blanket systems to be designed. The specific values of the operating temperatures need to be combined with compatibility data for the candidate coolants (cf. section 13.4) to determine if the temperature window is reduced due to corrosion issues. One disadvantage with the high minimum operating temperatures of the Ta, Mo and W alloys is that they may require the use of high-performance, high-cost materials (e.g., Ni-based superalloys) in the power conversion piping external to the reactor.

Additional important issues which have not yet been fully considered in the selection of the structural materials for APEX include transmutation effects (long term activation and burnup of alloy elements), afterheat/safety issues (including volatization), and availability/proven resources.

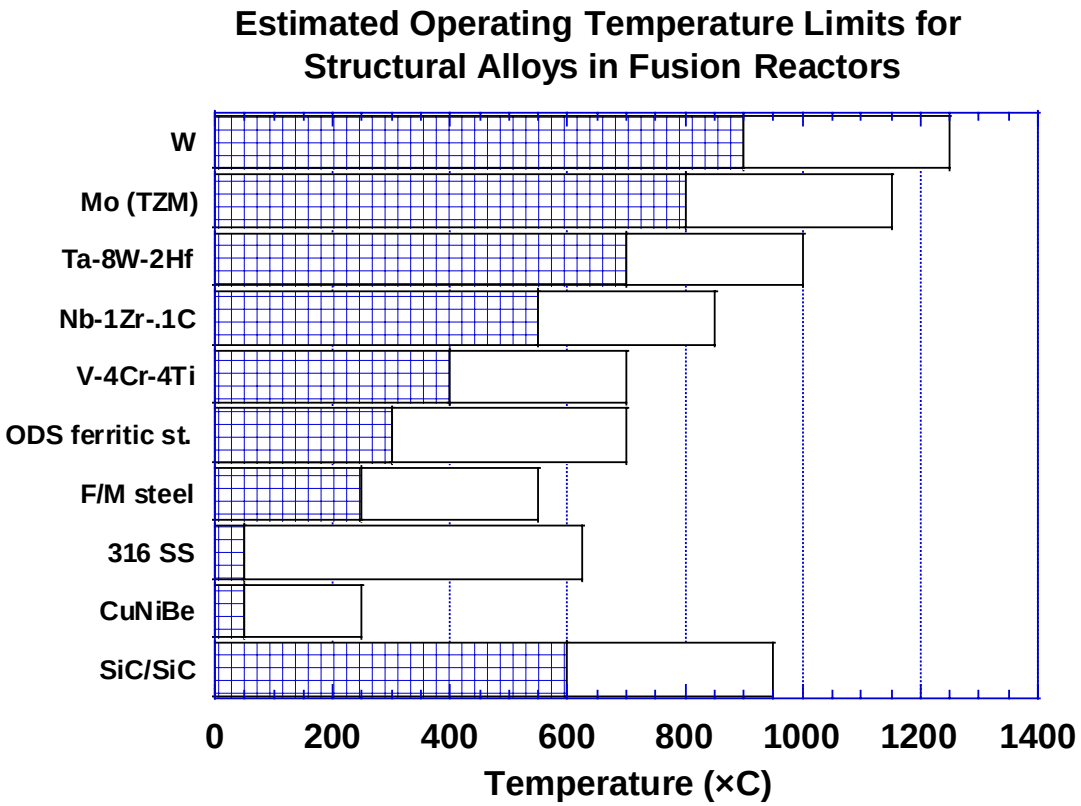

Fig. 13.6. Estimated operating temperature limits for structural alloys in fusion reactors based on thermal creep and irradiation considerations (see text). Chemical compatibility issues may cause a further restriction in the operating temperature window.

The list of recommended materials R&D activities for the next 1-3 years includes:

- chemical compatibility of coolants and structural materials at high temperatures (oxygen, Flibe, Sn-Li, including oxidation resistant alloys such as Mo-Ti-Si, intermetallics);
- measurement of thermophysical properties for Sn-20Li
- effect of coolant velocity on the erosion of structural materials (determination of the upper limit for coolant velocity)
- unirradiated and irradiated fracture toughness of refractory metals at APEX-relevant (high) temperatures;
- joining methods for refractory and oxide dispersion-strengthened alloys (stir friction welding, etc.)

Chapter 13 References

[1] S.J. Zinkle, in: Fusion Materials Semiann. Prog. Report for period ending Dec. 31 1997, DOE/ER-0313/23 (Oak Ridge National Lab, 1997) p. 99.

[2] S.J. Zinkle, A.F. Rowcliffe, C.O. Stevens, in: Fusion Materials Semiann. Prog. Report for period endingJune 30 1998, DOE/ER-0313/24 (Oak Ridge National Lab, 1998) p. 11.

[3] S.J. Zinkle, J.P. Robertson, R.L. Klueh, in: Fusion Materials Semiann. Prog. Report for period ending June 30 1998, DOE/ER-0313/24 (Oak Ridge National Lab, 1998) p. 135.

[4] S.J. Zinkle, L.L. Snead, in: Fusion Materials Semiann. Prog. Report for period ending June 30 1998, DOE/ER-0313/24 (Oak Ridge National Lab, 1998) p. 93.

[5] J.W. Davis, in: ITER Material Properties Handbook, ITER Document No. S74 MA 2 97-12-12 R 0.2, 4th ed, 1997.

[6] T.E. Tietz, J.W. Wilson, Behavior and Properties of Refractory Metals, Stanford University Press, Stanford, CA, 1965.

[7] D.C. Goldberg, in: Aerospace Structural Metals Handbook, AFML-TR 68-115, ed. W.F. Brown, Jr., (Metals and Ceramics Information Center, Battelle Columbus Laboratories, 1969).

[8] J.B. Conway, in: Proc. Symp. on Refractory Alloy Technology for Space Nuclear Power Applications, CONF-8308130, eds. R.H. Cooper, Jr., E.E. Hoffman, (Oak Ridge National Lab, 1984) p. 252.

[9] R.W. Buckman, Jr., in: High Temperature Silicides and Refractory Alloys, eds. C.L. Briant et al., MRS Symposium Proceedings vol. 322 (Materials Research Society, Pittsburgh, 1994) p. 329.

[10] S.J. Zinkle, W.S. Eatherly, in: Fusion Materials Semiannual Progress Report for Period ending June 30, 1997, DOE/ER-0313/22 (Oak Ridge National Lab, 1997) p. 143.

[11] S.J. Zinkle, W.S. Eatherly, in: Fusion Materials Semiannual Progress Report for Period ending Dec. 31, 1996, DOE/ER-0313/21 (Oak Ridge National Lab, 1996) p. 165.

[12] D.J. Alexander, S.J. Zinkle, A.F. Rowcliffe, in: Fusion Materials Semiannual Progress Report for Period ending Dec. 31, 1996, DOE/ER-0313/21 (Oak Ridge National Lab, 1996) p. 175.
[13] F.W. Wiffen, in: Proc. Symp. on Refractory Alloy Technology for Space Nuclear Power Applications, CONF-8308130, eds. R.H. Cooper, Jr., E.E. Hoffman, (Oak Ridge National Lab, 1984) p. 252.
[14] B.L. Cox, F.W. Wiffen, J. Nucl. Mater. 85&86 (1973) 901.
[15] F.W. Wiffen, in: Proc. Int. Conf. on Defects and Defect Clusters in BCC Metals and Their Alloys, Nuclear Metallurgy Vol. 18, ed. R.J. Arsenault, (National Bureau of Standards, Gaithersburg, MD, 1973) p. 176.
[16] O.P. Maksimkin, Phys. Met. Metallogr. 80 (1995) 592.
[17] L.L. Snead, S.J. Zinkle, D.J. Alexander, A.F. Rowcliffe, J.P. Robertson, W.S. Eatherly, in: Fusion Materials Semiann. Prog. Report for period ending Dec. 31 1997, DOE/ER-0313/23 (Oak Ridge National Lab, 1997) p. 81.
[18] S.J. Zinkle et al., J. Nucl. Mater. 258-263 (1998) 205.
[19] A. Hasegawa, K. Abe, M. Satou, C. Namba, J. Nucl. Mater. 225 (1995) 259.
[20] A. Hasegawa, K. Ueda, M. Satou, K. Abe, J. Nucl. Mater. 258-263 (1998) 902.
[21] J.M. Steichen, J. Nucl. Mater. 60 (1976) 13.
[22] V. Chakin, V. Kazakov, J. Nucl. Mater. 233-237 (1996) 902.
[23] S.A. Fabritsiev, A.S. Pokrovsky, J. Nucl. Mater. 252 (1998) 216.
[24] H. Kurishita, Y. Kitsunai, T. Shibayama, H. Kayano, Y. Hiraoka, J. Nucl. Mater. 233-237 (1996) 557.
[25] I.V. Gorynin et al., J. Nucl. Mater. 191-194 (1992) 421.
[26] P. Krautwasser, H. Derz, E. Kny, High Temperatures-High Pressures 22 (1976) 25.
[27] Y. Kitsunai, H. Kurishita, H. Kayano, Y. Hiraoka, T. Igarashi, T. Takida, J. Nucl. Mater. 271&272 (1999) 423.
[28] J.C. Batty, R.E. Stickney, J. Chem. Phys. 51 (1969) 4475.
[29] P.O. Schissel, O.C. Trulson, J. Chem. Phys. 43 (1965) 737.
[30] J.B. Berkowitz-Mattuck, A. Buchler, J.L. Engelke, S.N. Goldstein, J. Chem. Phys. 39 (1963) 2722.
[31] W.C. Steele, Avo, Wilmington, MA Report Tech. Rept. AFML-TR-65-343, Pt. II (1967).
[32] Y.G. Ptushinskii, B.A. Chuikov, Surf. Sci. 6 (1967) 42.
[33] W. Engelmaier, R.E. Stickney, Surf. Sci. 11 (1968) 370.
[34] W. Geaves, R.E. Stickney, Surf. Sci. 11 (1968) 395.
[35] S. Yamamoto, R.E. Stickney, Bulletin of the American Physical Society 14 (1969) 788.
[36] W.L. Worrell, J. Chipman, in: High Temperature Refractory Metals: Metallurgical Society Conf. 34, Part I, ed. W.A. Krivsky, (Gordon & Breach, New York, 1965) p. 335.
[37] B.A. Loomis, O.N. Carlson, in: Reactive Metals, ed. W.R. Clough, (Interscience, London, 1959) p. 227.
[38] H.D. Röhrig, J.R. DiStefano, L.D. Chitwood, J. Nucl. Mater. 258-263 (1998) 1356.
[39] B.A. Pint, P.M. Rice, L.D. Chitwood, J.H. DeVan, J.R. DiStefano, in: Fusion Materials Semiann. Prog. Report for period ending June 30 1998, DOE/ER-0313/24 (Oak Ridge National Lab, 1998) p. 77.

[40] K. Natesan, W.K. Soppet, M. Uz, J. Nucl. Mater. 258-263 (1998) 1476.
[41] H. Nakajima, S. Nagata, H. Matsui, S. Yamaguchi, Philos. Mag. A 67 (1993) 557.
[42] M. Uz, K. Natesan, V.B. Hang, J. Nucl. Mater. 245 (1997) 191.
[43] S. Malang, R. Mattas, Fusion Eng. Design 27 (1995) 399.
[44] O.K. Chopra, D.L. Smith, J. Nucl. Mater. 155-157 (1988) 715.
[45] P.F. Tortorelli, J. Nucl. Mater. 155-157 (1988) 722.
[46] P.F. Tortorelli, J. Nucl. Mater. 191-194 (1992) 965.
[47] M. Broc, T. Flament, P. Fauvet, J. Sannier, J. Nucl. Mater. 155-157 (1988) 715.
[48] J.R. DiStefano, J.H. DeVan, J.R. Keiser, R.L. Klueh, W.P. Eatherly, Oak Ridge National Lab Report ORNL/TM-12925/R1 (1995).
[49] J.R. Keiser, J.H. DeVan, E.J. Lawrence, J. Nucl. Mater. 85&86 (1979) 295.
[50] K. Natesan, C.B. Reed, R. Mattas, Fusion Eng. Design 27 (1995) 457.
[51] O.K. Chopra, D.L. Smith, J. Nucl. Mater. 155-157 (1988) 683.
[52] H. Feuerstein, H. Gräbner, J. Oschinski, S. Horn, J. Nucl. Mater. 233-237 (1996) 1383.
[53] J.H. DeVan, J.R. DiStefano, E.E. Hoffman, in: Proc. Symp. on Refractory Alloy Technology for Space Nuclear Power Applications, CONF-8308130, eds. R.H. Cooper, Jr., E.E. Hoffman, (Oak Ridge National Lab, 1984) p. 34.
[54] J.R. DiStefano, J. Mater. Eng. 11 (1989) 215.
[55] J. Saito, S. Inoue, S. Kano, T. Yuzawa, M. Furui, M. Morinaga, J. Nucl. Mater. 264 (1999) 216.
[56] H. Shimotake, N.R. Stalica, J.C. Hesson, Transaction ANS 10 (1967) 141.
[57] W.D. Manley et al., in: Progress in Nuclear Energy, Series IV, vol. 2, eds. R. Hurst, R.N. Lyon, C.M. Nicholls, (Pergamon Press, New York, 1960) p. 164.
[58] J. Saito, M. Morinaga, S. Kano, M. Furui, K. Noda, J. Nucl. Mater. 264 (1999) 206.
[59] J.W. Koger, A.P. Litman, Oak Ridge National Lab, Oak Ridge, TN Report ORNL-TM-2724 (1969).
[60] Y. Desai, K. Vedula, A.K. Misra, Journal of Metals 40 (1988) A63.
[61] J.W. Cree, M.F. Amateau, J. Am. Ceram. Soc. 70 (1987) C318.
[62] P. Hubberstey, T. Sample, J. Nucl. Mater. 248 (1997) 140.
[63] J.S. Tulenko, G. Schoessow, Transaction ANS 75 (1996) 72.
[64] J.R. Lance, G.A. Kemeny, Trans. Metall. Soc. AIME and Trans. Quarterly ASM 56 (1963) 204.
[65] H. Shimotake, J.C. Hesson, Transaction ANS 8 (1965) 413.
[66] F.L. LaQue, H.R. Copson, Corrosion resistance of metals and alloys, 2nd Ed., ACS Monograph #158: Reinhold, 1963, pp. 721.
[67] T.A. Coultas, Report NAA-SR-192 (1952).
[68] E.L. Reed, J. Am. Ceram. Soc. 37 (1954) 146.
[69] L.R. Kelman, et. al., Argonne National Laboratory, Argonne, IL Report ANL-4417 (1950).
[70] R.N. Lyon, Liquid metals handbook, 2nd Ed.: US Office of Naval Research, 1952, p. 148.
[71] B.D. Craig, D.S. Anderson, ASM Handbook of corrosion data, 2nd Ed.. Materials Park, OH: ASM International, 1995, p. 496.